13th International Symposium on Particle Image Velocimetry – ISPIV 2019
Munich, Germany, July 22-24, 2019

Experimental analysis of Rayleigh-Bénard convection in a cylindrical cell by tomographic PIV

Gerardo Paolillo[1]*, Carlo Salvatore Greco[1], Tommaso Astarita[1], Gennaro Cardone[1]

[1]Università degli Studi di Napoli "Federico II", Dipartimento di Ingegneria Industriale, Napoli, Italia

*gerardo.paolillo@unina.it

Abstract

This paper presents an experimental investigation of Rayleigh-Bénard convection in both rotating and non-rotating conditions. Rayleigh-Bénard convection, the fluid flow driven by temperature gradients parallel to the gravity, is relevant to a great variety of physical phenomena, ranging from motions in the atmosphere and the oceans to convection in the interior of planets and stars. In many of these applications, the interplay between a background rotation and the thermal convection has a key role in the fluid dynamic behaviour of the system. In the present work, the time-resolved tomographic particle image velocimetry (PIV) is used to investigate the whole domain of Rayleigh-Bénard convection inside a cylinder with aspect ratio equal to $1/2$ at Rayleigh and Prandtl numbers equal to 1.86×10^8 and 7.6, respectively. The effects of rotation on the flow dynamics and evolution are also investigated in similar operating conditions at two different Rossby numbers, namely 0.25 and 0.1. The behaviour of the turbulent flow is analyzed both in the time-average and instantaneous evolution with focus on the large scale structures of the flow. Modal decomposition techniques are also used to identify the characteristic modes of the thermal convection.

1 Introduction

Rayleigh-Bénard (RB) convection is the fluid flow induced by the buoyancy forces due to temperature gradients parallel to the gravity. Such a phenomenon occurs in many natural processes, such as oceanic current and winds (Rahmstorf, 2006), convection in the Earth's inner core (Glatzmaier and Roberts, 1995) and also plate tectonics (which is driven by the convective motions in the Earth's mantle) (Morgan, 1972; Richter, 1978). In such geophysical applications, the flow dynamics is also significantly influenced by the planet rotation via the occurrence of the Coriolis and centrifugal forces. On the application side, rotating RB convection is involved in the cooling process of the turbine blades in turbomachinery (Johnston, 1998) and in the separation of carbon dioxide (CO_2) from methane or nitrogen gas (van Wissen et al., 2006). Furthermore, theoretical studies of RB convection have been fundamental in the fields of hydrodynamic stability (Chandrashekhar, 1981; Drazin and Reid, 1981) and pattern formation (Getling, 1998).

In recent years, the development of non-intrusive high-fidelity flow visualization techniques, such as particle image velocimetry (PIV) or laser induced fluorescence (LIF), but also the advent of high-speed supercomputers that enabled the direct numerical simulation (DNS) of very turbulent flows, have made it possible to get a better insight into the complex and chaotic dynamics of the flow structures of RB convection and their relationship with the related heat transfer. The latest works in this direction have focused on the thermal convection in confined geometries, like cylinders or rectangular boxes, since in the latter case it is possible to reproduce exactly the same boundary conditions and thus fairly compare results from different experimental, numerical and theoretical investigations. In particular, the cylindrical geometry has gained much attention because it presents a direction of statistical symmetry, the azimuthal one (Ahlers et al., 2009; Xia, 2013).

Within the Oberbeck-Boussinesq approximation, the space of the control parameters for the non-rotating RB convection is very narrow and consists of only three parameters: the Rayleigh number $Ra = \beta g L^3 \Delta T / (\alpha \nu)$, the Prandtl number $Pr = \nu/\alpha$ and the aspect ratio $\Gamma = D/L$, where β, ν and α are the thermal expansion coefficient, kinematic viscosity and thermal diffusivity of the fluid, L and D the height and the internal diameter of the cylinder, ΔT the temperature difference across the cell. The effects of a rotation around the

cylinder axis with magnitude equal to Ω are determined by only two dimensionless numbers: the Rossby number $Ro = \sqrt{\beta \Delta g/L}/(2\Omega)$ and the Froude number $Fr = \Omega^2 D/(2g)$, which measure the importance of the buoyancy and the centrifugal forces with respect to the inertial ones, respectively. In most applications, $Fr \ll 1$ and the centrifugal effects are in fact negligible.

It is well-known that the convective motion in both the non-rotating and the rotating case arises after an overturning instability of the thermal fluid layer above a critical value of the Rayleigh number. In such a regime, hot and cold plumes detach from the thin boundary layers on the top and the bottom plates and organize into a large-scale circulatory stream, the so-called large scale circulation (LSC), with a quasi-planar flywheel structure (Qiu and Tong, 2001). In a cylindrical cell with $\Gamma = 1$ (height equal to internal diameter), the LSC exhibits a very chaotic behaviour characterized by a continual re-orientation of its plane (Brown and Ahlers, 2006; Xi et al., 2006) and multiple oscillatory modes, namely a torsional mode (Funfschilling and Ahlers, 2004), a sloshing mode (Zhou et al., 2009) and cessations and reversals of the circulation direction (Brown and Ahlers, 2006; Xi and Xia, 2007), which alternate in a random sequence. As concerns slender cylinders ($\Gamma < 1$), the flow evolution is still more complex and the LSC has been observed to switch between different states. In their DNS investigation in the case $\Gamma = 1/2$, Verzicco and Camussi (2003) found out the existence of a flow mode consisting of two vertically-stacked near-circular counter-rotating rolls, which were later observed experimentally by Xi and Xia (2008). The latter study revealed random temporal successions of one-roll and double-roll states, with a prevalent occurrence of the two-roll state as Γ is decreased. In the work by Stringano and Verzicco (2006) a simple model for the prediction of this bimodality was also given.

The addition of a background rotation substantially modifies both the flow dynamics and the heat transfer of the RB convection (refer to Stevens et al. (2013) for a throughout review on this topic). In particular, three different regimes can be distinguished in the behaviour of the Nusselt number *Nu* (i.e., non-dimensional global heat transfer across the cell) as a function of the Rossby number: a regime of weak rotation (high *Ro*), in which *Nu* does not change with increasing *Ro*; a regime of moderate rotation (intermediate *Ro*), in which *Nu* exhibits a monotonic increase with *Ro*; a regime of strong rotation (low *Ro*), in which *Nu* shows an abrupt drop with increasing *Ro*.

From a dynamical standpoint, the two perhaps most interesting features that have been observed are the precession of the LSC in the direction opposite to the background rotation (Hart et al., 2002; Kunnen et al., 2008) and the increase in the frequency of cessations (Zhong and Ahlers, 2010). The regimes of moderate and strong rotation are characterized by the breakdown of the LSC and the emergence of vertically-aligned vortices, often denoted as Taylor-Proudman columns (Stevens et al., 2009; Weiss et al., 2010).

The above discussion elucidates that three-dimensional measurements are mandatory for the analysis of RB convection due to its inherent turbulent nature. In the present work, the time-resolved tomographic particle image velocimetry (PIV) is used to investigate the whole domain of RB convection inside a cylinder with aspect ratio equal to $1/2$ at Rayleigh and Prandtl numbers equal to 1.86×10^8 and 7.6, respectively. The effects of rotation on the flow dynamics and evolution are also investigated in similar operating conditions at two different Rossby numbers, namely 0.25 and 0.1.

2 Experimental setup

2.1 Apparatus

The experimental tomographic PIV setup is shown in Fig. 1. The convection cell is a Plexiglas cylinder filled with water and immersed in a water tank. The bottom heating system consists of an electrolytic copper insert connected to a mica-insulated flat heater, which can provide a heating power up to 100 W. The copper insert is made of two parts in between which a PT100 1/10-DIN RTD sensor (Omega RTD-3-F3105-80-T-1/10) is embedded. The top cooling system consists of a water heat exchanger obtained by assembling a set of Plexiglas layers. These layers comprise two recirculation chambers with nearly opposite tangential inlet and outlet, delimited by a thin slab with a small central hole and separated by the convection cell via a Plexiglas foil of 0.25 mm thickness, which ensures a negligible temperature drop across it. The water is refrigerated by a Peltier thermoelectric cooler and pumped into the lower recirculation chamber. The tubes of the water circuit are covered by neoprene rubber coating in order to limit heat losses due to heat transfer with the surrounding ambient. The water temperature is measured at the heat exchanger inlet by means of an immersion ultra-precise PT100 1/10-DIN RTD sensor (Omega P-M-1/10-1/8-6-1/4-P-6). Both temperatures are kept constant by a thermoelectric controller (TEC) with a stability up to 0.01°C. The TEC (Meerstetter Engineering TEC-1123-HV) performs a PID control by adjusting the current inputs to the flat heater and the Peltier element.

The temperature of the water in the tank is measured by means of an immersion PT100 1/10-DIN RTD probe (Omega P-M-1/10-1/8-6-0-P-6) and can be controlled by a specifically designed system. The latter consists of a water circuit comprising a pump, a Peltier cooling device and two loop tubes immersed in the tank: water can be withdrawn from the bottom of the tank, refrigerated by the Peltier device and pumped back to the tank from the top. This generates a convective motion outside of the cylindrical sample, which allows to maintain the temperature of the external side of its wall constant at the tank bulk temperature, set to the intermediate value between the top and the bottom temperatures.

The imaging system consists of a Nd:YAG laser, operated at 7.5 Hz, and four sCMOS cameras (Andor Zyla, 5.5 megapixels). The laser light is shaped, through an appropriate system of mirrors and lenses, into a cylindrical beam that passes through the transparent heat exchanger on the top of the cell and illuminates the entire convection domain. The four cameras are arranged in an angular configuration with a constant spacing of 40° and equipped with 28 mm focal length objectives set at f-number equal to 22 (the resulting digital resolution is 14 vox/mm for the non-rotating case and 15 vox/mm for the rotating ones).

The seeding particles are orange fluorescent polyethylene microspheres (Cospheric UVPMS-BO-1.00) with average diameter of 58 μm and density of 1.00 g/cm^3, resulting in a relaxation time lower than 1 ms (which is significantly below the turbulent dissipative time scales of the thermal convection at the currently investigated conditions). Fluorescence of the particles is exploited to reduce the green reflections from the copper base and increase the particle contrast. For this purpose, the camera lenses are equipped with HOYA YA3 orange filters.

In the rotating experiments all the equipment, except the laser, is placed on a rotating table which is operated at angular velocities greater than 30°/s. The rotating table is driven by a synchronous brushless motor (STIMA MIRA 71b6 B5) with 6 poles (1000 rpm), a nominal power of 0.73 kW and an efficiency of 83.1%. The motor is piloted by an inverter (Sinus H 0002 4T BA2K2) that performs a vector control to ensure stability of the angular velocity up to 0.5% of the mean value. The rotation is transmitted through a gear box connected to the motor and a system of two wheels with a toothed belt. A mercury slip ring with six conductors (Mercotac 630, 4-30 A per conductor, 0-250 V AC/DC) is installed on the rotating shaft for power transmission to the computer.

2.2 Image processing

In all the investigated cases, measurements are carried out over about four hours with a sampling frequency of 7.5 Hz (corresponding to a sequence of 108,000 snapshots). This is sufficient to carry out a time-resolved analysis of the particle images and exploit the advantages of some modern approaches for particle tracking velocimetry, namely 'Shake-the-Box' (Schanz et al., 2016) and the iterative particle reconstruction method (Wieneke, 2012).

Time-resolved motion analysis consists essentially of two steps. Initially, a first set of snapshots (typically 5-10) is analyzed by the sequential-motion-tracking enhancement (SMTE) algorithm (Lynch and Scarano, 2015). At this stage, the light intensity distribution is reconstructed with multiple iterations of the

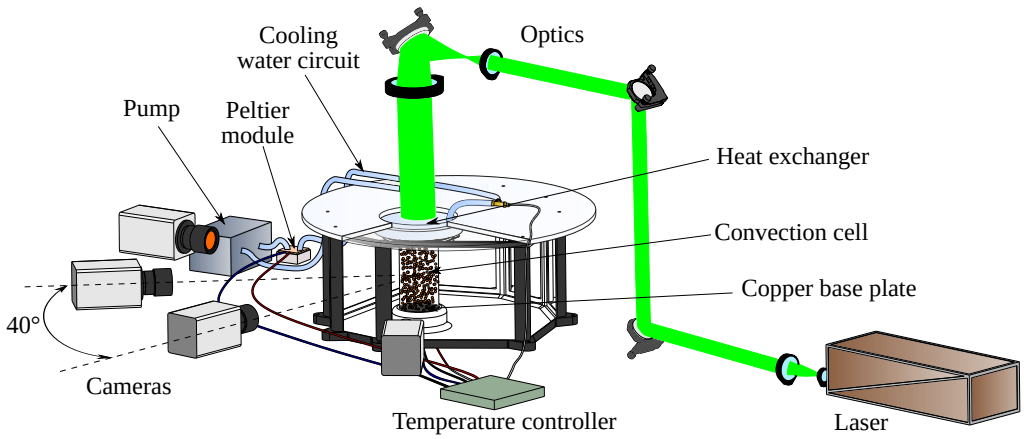

Figure 1: Schematic representation of the tomographic PIV setup.

SMART (Atkinson and Soria, 2009) and CSMART (Ceglia et al., 2014; Castrillo et al., 2016) algorithms, using a multi-resolution approach (Discetti and Astarita, 2012a); multi-pass volumetric cross-correlations are performed with an efficient algorithm using sparse matrices (Discetti and Astarita, 2012b). In the second phase of the process, the STB method (Schanz et al., 2016) is used for particle tracking. Particle triangulation is performed by iterative particle identification (Wieneke, 2012), while forward-time projection of particles is based on both extrapolation of known trajectories and cross-correlation.

The output of the above process consists of the particle trajectories, which are subsequently interpolated onto a structured grid comprised within the measurement volume. The interpolation is based on least-squares polynomial fitting of local data: for each point of the grid, particles falling within a fixed search radius are identified and the velocities of such particles are used to determine a local polynomial fitting function which is then evaluated at the location of the grid point. Moreover, to reduce the effects of the ghost particles on the determination of the velocity field, only particles with trajectories longer than a fixed number of time instants are used in the above procedure. For the present experiments, we use a search radius of 30 voxels (about 2 mm) and a second-order polynomial function for the fit and employ only particles with trajectories longer than 7 time instants.

3 Results and discussion

Figure 2 shows the structure of the time-averaged velocity field in the case of $Ra = 1.86 \times 10^8$ and $Pr = 7.6$. In agreement with the work by Sun et al. (2005) and Verzicco and Camussi (2003), this is found to be azimuthally axisymmetric. Figure 2a reports the contour map of the non-dimensional vertical velocity component in one of the azimuthal planes containing the cylinder axis (namely the xz-plane); the velocity scale is the free-fall velocity $u_0 = \sqrt{\beta \Delta T g L}$, which is 38.2 mm/s in the present case. In the upper half of the cylinder, the mean flow is observed to fall down in the regions adjacent to the sidewalls and rise up in the central part, while an opposite behaviour is observed in the lower part. This results in a radial recirculation in both the halves of the cell, with the formation of two toroidal vortex structures near the top and bottom plates, shown in Fig. 2b via the (green) isosurfaces of Q (second invariant of the velocity gradient tensor), along with the isosurfaces of the vertical velocity component corresponding to values of $\pm 0.026\, u_0$ (red and blue for positive and negative, respectively).

The observed structure of the flow field is strictly connected to the dynamics of the plumes and the LSC. In fact, the region of positive (negative) vertical velocities adjacent to the cylinder sidewall in the lower (upper) half of the cell is related to hot (cold) plumes detaching from the thermal boundary layer on the bottom (top) plate and rising upward (falling down); conversely, the central region of negative (positive) velocities is associated with the arrival of the plumes coming from the opposite plate. The structure of the instantaneous flow field is not axisymmetric, with the plumes organized in a LSC localized in a nearly vertical plane, which is subject to continual reorientation over the time.

The main large-scale structures of the velocity field can be detected by proper orthogonal decomposition (POD) of the fluctuating part of the velocity field. The first two POD modes are shown in Fig. 3: specifically, Figure 3a-b report the isosurfaces of the vertical velocity component, while in Fig. 3c the map of the vertical velocity in the xz-plane with the 2D streamlines superimposed for the 2nd mode is drawn. In both modes, we note two vertical currents forming a domain-filling circulation, in the following referred to as single roll state or structure (SRS). It is noted that the SRS has a quasi-planar structure and is not tilted with respect to the cylinder axis; moreover, four small counter-rotating rolls are observed in the corners between the SR and the plates. This pattern has to be considered as the main contribution to the LSC existing in the instantaneous evolution. A remarkable difference between the SR of the first two modes and the LSC is that the latter has a significant inclination with respect to the cylinder axis, as observed in the present investigation and also previous works (e.g., Sun et al., 2005). Indeed, the inclination of the LSC results from the combination of the mean velocity field (Fig. 2) and the first two modes.

It is also very interesting to note that the first two POD modes have exactly the same structure except for a rotation of about 90° about the cylinder axis. Such a feature can be explained by considering that the combination of these two modes can result practically in any azimuthal orientation of the LSC plane in the instantaneous flow field. The pairing of the first two POD modes is also confirmed by their energetic levels, which are observed to be comparable (although not shown here).

Analogously, the 3rd and 4th modes (Fig. 4) appear to be paired. They are characterized by the presence of two counter-rotating large-scale rolls laying approximately in the same azimuthal plane, as clearly detectable from the 2D streamlines of the 4th mode in the xy-plane (Fig. 4c). These POD modes resemble considerably the double roll state (DRS) observed in cylindrical samples with aspect ratio lower than 1 (e.g.,

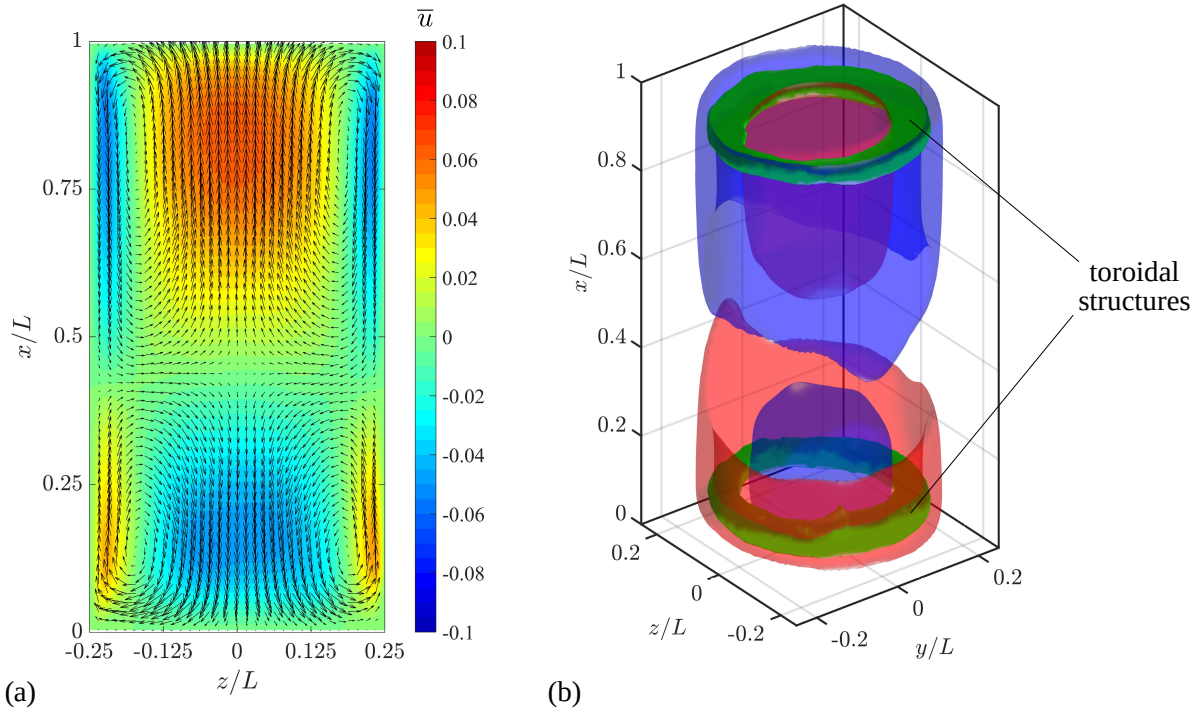

Figure 2: Mean velocity flow field: (a) vertical velocity component map with vectors superimposed (velocity are scaled by the free fall velocity u_0); (b) isosurfaces of the vertical velocity component corresponding to values of $\pm 0.026 u_0$ (red and blue for the positive and negative values, respectively) and isosurfaces of the second invariant of the velocity gradient field showing the mean vortical structures, corresponding to approximately 10% of the maximum value.

Verzicco and Camussi, 2003). Indeed, the emergence of the latter in the instantaneous evolution is generally associated with a weak correlation of the instantaneous velocity field with the first POD modes (i.e., a small value of the projection of the snapshot onto these POD modes). However, when both the contributions of the first and the second pair of POD modes are significant, the addition of the 3rd and the 4th POD modes results in a torsion of the LSC.

Measurements of the rotating RB convection are presented for slightly different values of Ra and Pr with respect to the non-rotating case, i.e. for $Ra = 2.86 \times 10^8$ and $Pr = 6.4$. Figure 5 reports the time-averaged maps of the axial, radial and azimuthal velocity components for $Ro = 0.25$ and $Ro = 0.1$. In this case, the mean velocity fields have been azimuthally averaged to allow an analysis of the different behaviours in the central part and the near-sidewall regions of the flow field. In the flow field at $Ro = 0.25$ (Fig. 5a-c), the radial velocity component is found to be significantly smaller than the axial and the tangential ones. This results in the absence of a large-scale coherent pattern, although considerably high radial outward velocities are found near the top plate. From the inspection of the vertical velocity field it is possible to detect a radial recirculation in the region adjacent to the sidewall with downward velocities close to sidewall and positive velocities at smaller radial distances from the cylinder axis. It should be noted that however such a recirculation is not planar since it is associated with the azimuthal velocities shown in Fig. 5c. In particular, a cyclonic rotation (characterized by positive azimuthal velocities) is observed in the upper part of the cylinder, whereas an anticyclonic rotation occurs in the lower one. In the central part of the convection cell vertical flow towards the plates is observed, probably due to the Ekman suction mechanism.

At the lower Rossby number ($Ro = 0.1$), smaller velocity values are observed. In particular, both the axial and the radial velocities are found to be very small compared to the azimuthal velocities (about one order of magnitude). The distribution of the azimuthal velocity is not very different from that observed at $Ro = 0.25$: it is possible to detect again an anticyclonic motion in the lower half of the cylinder and a cyclonic motion in the upper half. However, at a closer look it is possible to see that the central part of the convection cell is characterized mainly by positive azimuthal velocities. It should also be remarked that in this case no radial recicurlation is indeed observed in the mean evolution; conversely, negative vertical

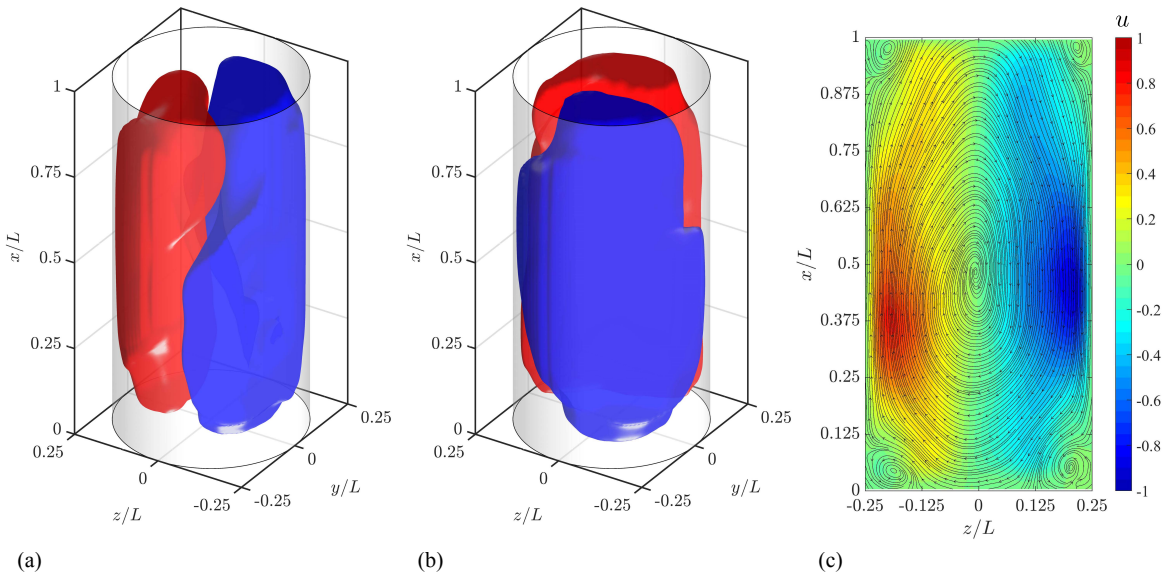

Figure 3: First pair of POD modes. 3D isosurfaces of the vertical velocity component corresponding to values of $\pm 10\%$ of the maximum for (a) the 1st and (b) the 2nd mode (red corresponds to the positive value) and (c) contour map of the vertical velocity component in the xz-plane for the 2nd mode. Values are scaled by the maximum of the vertical velocity component.

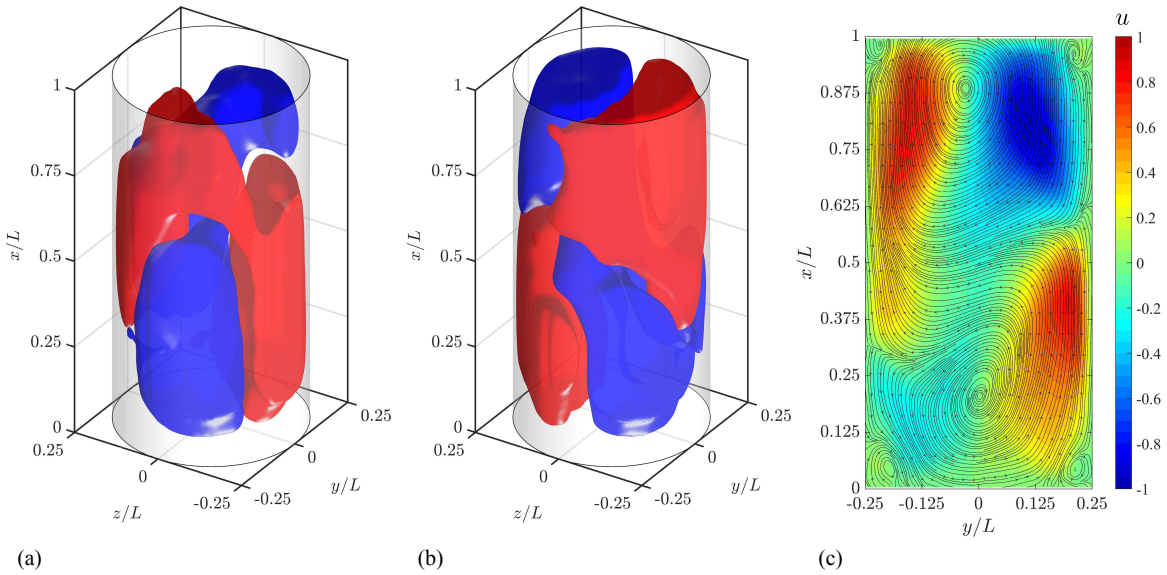

Figure 4: Second pair of POD modes. 3D isosurfaces of the vertical velocity component corresponding to values of $\pm 10\%$ of the maximum for (a) the 3rd and (b) the 4th mode (red corresponds to the positive value) and (c) contour map of the vertical velocity component in the xy-plane for the 4th mode. Values are scaled by the maximum of the vertical velocity component.

velocities are found in the lower half of the cylinder, while positive vertical velocities occur over the upper half.

Figure 6 reports a comparison between the instantaneous velocity fields related to the cases $Ro = 0.25$ and $Ro = 0.1$ at selected times. The large-scale coherent structures are identified by the Q-criterion, using the same threshold. As regards $Ro = 0.25$, the coherent structures of the flow field (Fig. 6a) have the appearance of thick columnar structures with a slightly twisted shape. For $Ro = 0.1$ (Fig. 6b), the characteristic

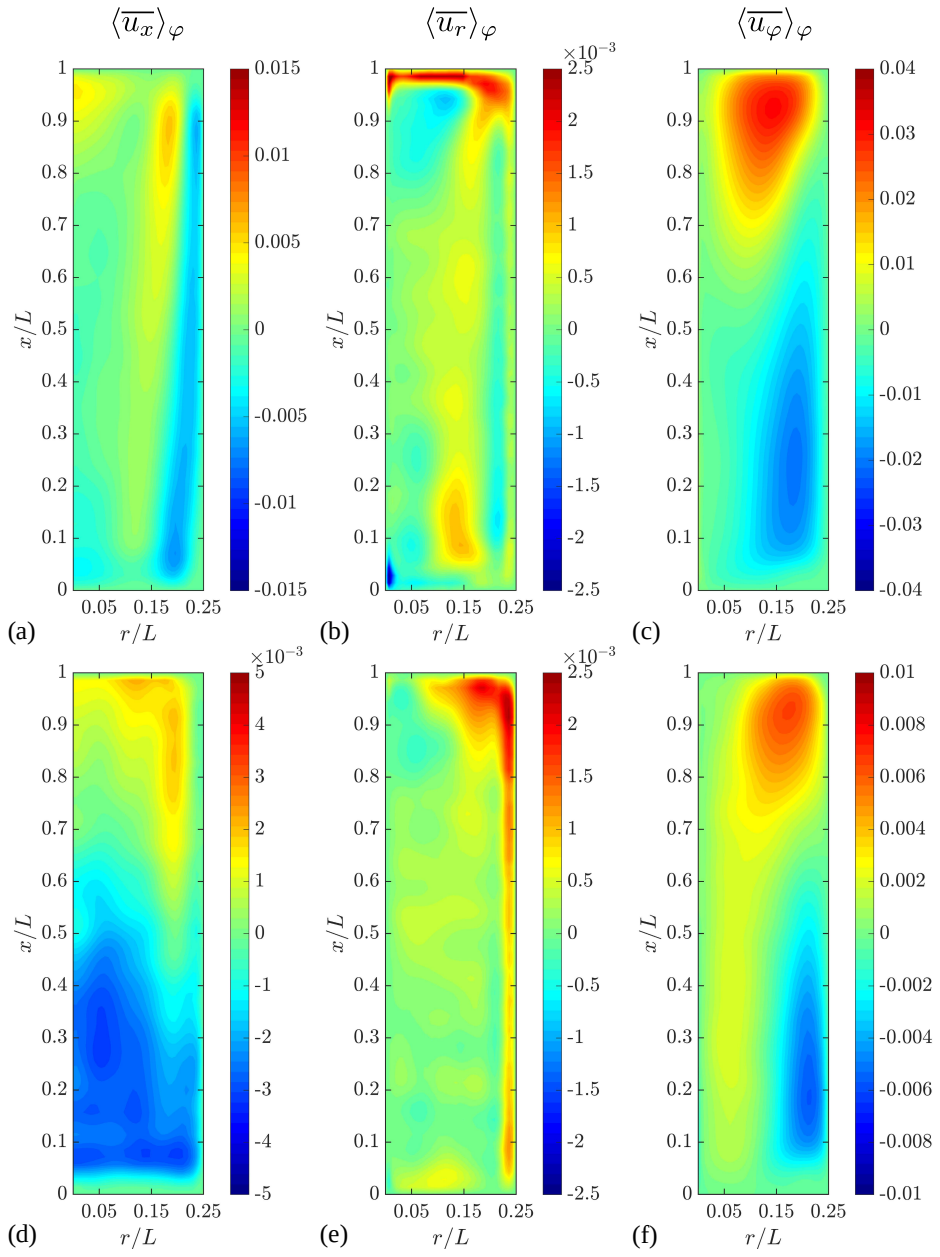

Figure 5: Experimental measurements of the rotating convection for $Ra = 2.86 \times 10^8$ and $Pr = 6.4$. From left to right, time- and azimuthally-averaged fields of the vertical, radial and azimuthal velocity components. The rows from top to bottom correspond to (a)-(c) $Ro = 0.25$ and (d)-(f) $Ro = 0.1$. Velocities are scaled by the free-fall velocity.

size of such structures is noticeably smaller, but this corresponds to an increased density of the structures themselves.

In conclusion, it should be noted that the current rotating measurements present a picture in disagreement with the available literature on the topic. For instance, the numerical investigation of Kunnen et al. (2011) carried out in a cylindrical sample with $\Gamma = 1$, $Ra = 1.00 \times 10^9$ and $Pr = 6.4$ features a very different flow behaviour in the mean evolution to that observed in the present study, in terms of the time-averaged evolution. Further investigation is surely needed to explain such discrepancies, although a relevant peculiarity of the present experiments is that the cylinder sidewall is not adiabatic, but isothermal at intermediate temperature between those of the top and the bottom. Therefore, it cannot be ruled out that the observed

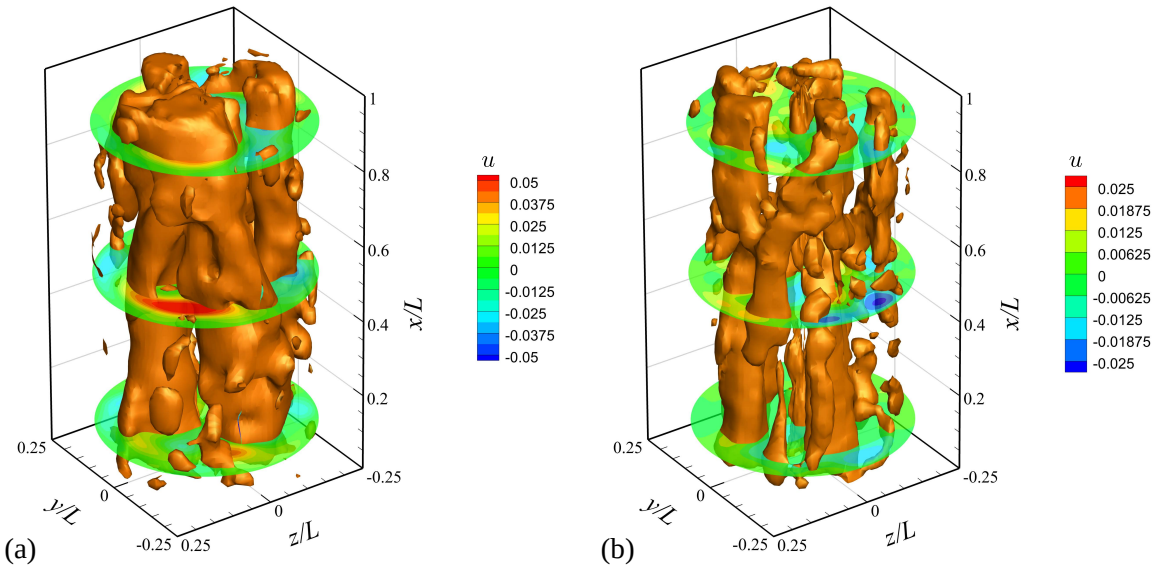

Figure 6: Comparison between numerical simulations and experimental results. Instantaneous velocity fields for $Ra = 2.86 \times 10^8$, $Pr = 6.4$ and (a) $Ro = 0.25$ and (b) $Ro = 0.1$. Slices of the vertical velocity component field at three different heights ($0.1L$, $0.5L$ and $0.9L$) and isosurfaces of Q. Velocities are scaled by the free-fall velocity.

flow evolution is influenced by the heat transfer across the lateral wall.

4 Conclusions

Three-dimensional measurements of the velocity field in Rayleigh-Bénard convection inside a cylinder with aspect ratio equal to $1/2$ in both rotating and non-rotating conditions have been carried out by using time-resolved tomographic particle image velocimetry.

In the non-rotating case, the mean velocity field has been found to exhibit axisymmetric structure in agreement with previous numerical and experimental investigations; this structure has been related to the quite complex dynamics of the LSC and plumes. The characteristic modes of the turbulent convection have been extracted by modal decomposition of the fluctuating velocity field. The first POD modes capture the principal states of the LSC that have been observed in previous numerical and experimental studies, but never, to the author's knowledge, in a 3D experimental investigation; also some of the oscillatory modes of the LSC are captured by the POD modes.

As concerns the investigation of the rotating RB convection, experimental measurements have been performed at $Ro = 0.25$ and $Ro = 0.1$. In both cases, the flow is organized in two counter-rotating azimuthal circulations extending over the upper and the lower halves of the cylindrical sample. For $Ro = 0.25$, such a behaviour is associated with a secondary radial recirculation near the cylinder sidewall with descending velocities in the very proximity of the wall. Finally, it is observed that, when rotation is added, the LSC circulation is replaced by columnar vortices, which extend from the bottom to the top of the cylindrical cell. The size of such structures is observed to decrease when increasing the background rotation; correspondingly, their concentration is observed to increase.

References

Ahlers G, Grossmann S, and Lohse D (2009) Heat transfer and large scale dynamics in turbulent Rayleigh-Bénard convection. *Reviews of Modern Physics* 81:503–537

Atkinson C and Soria J (2009) An efficient simultaneous reconstruction technique for tomographic particle image velocimetry. *Experiments in Fluids* 47:553

Brown E and Ahlers G (2006) Rotations and cessations of the large-scale circulation in turbulent Rayleigh–Bénard convection. *Journal of Fluid Mechanics* 568:351–386

Castrillo G, Cafiero G, Discetti S, and Astarita T (2016) Blob-enhanced reconstruction technique. *Measurement Science and Technology* 27:094011

Ceglia G, Discetti S, Ianiro A, Michaelis D, Astarita T, and Cardone G (2014) Three-dimensional organization of the flow structure in a non-reactive model aero engine lean burn injection system. *Experimental Thermal and Fluid Science* 52:164–173

Chandrashekhar S (1981) *Hydrodynamic and Hydromagnetic Stability*. Dover, New York

Discetti S and Astarita T (2012a) A fast multi-resolution approach to tomographic PIV. *Experiments in Fluids* 52:765–777

Discetti S and Astarita T (2012b) Fast 3D PIV with direct sparse cross-correlations. *Experiments in Fluids* 53:1437–1451

Drazin PG and Reid WH (1981) *Hydrodynamic stability*. Cambridge University Press, Cambridge, England

Funfschilling D and Ahlers G (2004) Plume motion and large-scale circulation in a cylindrical Rayleigh-Bénard cell. *Physical Review Letters* 92:194502:1–4

Getling AV (1998) *Rayleigh-Bénard Convection: Structures and Dynamics*. page 39. World Scientific, Singapore

Glatzmaier GA and Roberts PH (1995) A three-dimensional convective dynamo solution with rotating and finitely conducting inner core and mantle. *Physics of the Earth and Planetary Interiors* 91:63–75

Hart J, Kittelman S, and Ohlsen D (2002) Mean flow precession and temperature probability density functions in turbulent rotating convection. *Physics of Fluids* 14:955–962

Johnston JP (1998) Effects of system rotation on turbulence structure: a review relevant to turbomachinery flows. *International Journal of Rotating Machinery* 4:97–112

Kunnen R, Clercx H, and Geurts BJ (2008) Breakdown of large-scale circulation in turbulent rotating convection. *Europhysics Letters* 84:24001:1–6

Kunnen RP, Stevens RJ, Overkamp J, Sun C, van Heijst GF, and Clercx HJ (2011) The role of Stewartson and Ekman layers in turbulent rotating Rayleigh–Bénard convection. *Journal of Fluid Mechanics* 688:422–442

Lynch KP and Scarano F (2015) An efficient and accurate approach to MTE-MART for time-resolved tomographic PIV. *Experiments in Fluids* 56:66

Morgan WJ (1972) Deep mantle convection plumes and plate motions. *American Association of Petroleum Geologists Bulletin* 56:203–213

Qiu XL and Tong P (2001) Large-scale velocity structures in turbulent thermal convection. *Physical Review E* 64:036304

Rahmstorf S (2006) Thermohaline ocean circulation. in SA Elias, editor, *Encyclopedia of Quaternary Sciences*. pages 739–750. Elsevier, Amsterdam

Richter FM (1978) Mantle convection models. *Annual Review of Earth and Planetary Sciences* 6:9–19

Schanz D, Gesemann S, and Schröder A (2016) Shake-The-Box: Lagrangian particle tracking at high particle image densities. *Experiments in Fluids* 57:70

Stevens RJ, Clercx HJ, and Lohse D (2013) Heat transport and flow structure in rotating Rayleigh–Bénard convection. *European Journal of Mechanics - B/Fluids* 40:41–49

Stevens RJ, Zhong JQ, Clercx HJ, Ahlers G, and Lohse D (2009) Transitions between turbulent states in rotating Rayleigh-Bénard convection. *Physical Review Letters* 103:024503

Stringano G and Verzicco R (2006) Mean flow structure in thermal convection in a cylindrical cell of aspect ratio one half. *Journal of Fluid Mechanics* 548:1–16

Sun C, Xi HD, and Xia KQ (2005) Azimuthal symmetry, flow dynamics, and heat transport in turbulent thermal convection in a cylinder with an aspect ratio of 0.5. *Physical Review Letters* 95:074502:1–4

van Wissen R, Golombok M, and Brouwers JJH (2006) Gas centrifugation with wall condensation. *AlChE Journal* 52:1271–1274

Verzicco R and Camussi R (2003) Numerical experiments on strongly turbulent thermal convection in a slender cylindrical cell. *Journal of Fluid Mechanics* 477:19–49

Weiss S, Stevens RJ, Zhong JQ, Clercx HJ, Lohse D, and Ahlers G (2010) Finite-size effects lead to supercritical bifurcations in turbulent rotating Rayleigh-Bénard convection. *Physical Review Letters* 105:224501:1–4

Wieneke B (2012) Iterative reconstruction of volumetric particle distribution. *Measurement Science and Technology* 24:024008

Xi HD and Xia KQ (2007) Cessations and reversals of the large-scale circulation in turbulent thermal convection. *Physical Review E* 75:066307:1–5

Xi HD and Xia KQ (2008) Flow mode transitions in turbulent thermal convection. *Physics of Fluids* 20:055104:1–14

Xi HD, Zhou Q, and Xia KQ (2006) Azimuthal motion of the mean wind in turbulent thermal convection. *Physical Review E* 73:056312:1–13

Xia KQ (2013) Current trends and future directions in turbulent thermal convection. *Theoretical and Applied Mechanics Letters* 3:052001

Zhong JQ and Ahlers G (2010) Heat transport and the large-scale circulation in rotating turbulent Rayleigh–Bénard convection. *Journal of Fluid Mechanics* 665:300–333

Zhou Q, Xi HD, Zhou SQ, Sun C, and Xia KQ (2009) Oscillations of the large-scale circulation in turbulent Rayleigh–Bénard convection: the sloshing mode and its relationship with the torsional mode. *Journal of Fluid Mechanics* 630:367–390